Approach and separation of quantum vortices with balanced cores

C. Rorai[1], J. Skipper[2], R. M. Kerr[2], K. R. Sreenivasan[3]

[1]NORDITA, Stockholm, Sweden, rorai@nordita.org
[2]Department of Mathematics, University of Warwick, Coventry, UK CV4 7AL
[3]Department of Physics, New York University, NYC, NY 100xx

http://arxiv.org/abs/1410.1259

Using two innovations, smooth, but distinctly different, scaling laws for the numerical reconnection of pairs of initially orthogonal and anti-parallel quantum vortices are obtained using the three-dimensional Gross-Pitaevskii equations, the simplest mean-field non-linear Schrödinger equation for a quantum fluid. The first innovation suppresses temporal fluctuations by using an initial density profile that is slightly below the usual two-dimensional steady-state Padé approximate profiles. The second innovation is to find the trajectories of the quantum vortices from a pseudo-vorticity constructed on the three-dimensional grid from the gradients of the wave function. These trajectories then allow one to calculate the Frenet-Serret frames and the curvature of the vortex lines. For the anti-parallel case, the scaling laws just before and after reconnection obey the dimensional $\delta \sim |t_r - t|^{1/2}$ prediction with temporal symmetry about the reconnection time t_r and physical space symmetry about the x_r, the mid-point between the vortices, with extensions of the vortex lines formng the edges of an equilateral pyramid. For all of the orthogonal cases, before reconnection $\delta_{in} \sim (t - t_r)^{1/3}$ and after reconnection $\delta_{out} \sim (t - t_r)^{2/3}$, which are respectively slower and faster than the dimensional prediction. In these cases, the reconnection takes place in a plane defined by the directions of the curvature and vorticity. To define the structure further, lines are drawn that connect the four arms that extend from the reconnection plane, four angles θ_i between these arms are found, then summed, giving $\sum \theta_i > 360°$. This implies that the overall structure is convex or hyperbolic, as opposed to the acute angles of the anti-parallel pyramid.

Key words: Gross-Pitaevskii equations, Bose-Einstein condensate, quantum fluids, vortex reconnection

---

1. Background

The term "quantum turbulence" refers to a tangle of quantum vortex lines, a tangle whose formation and decay is determined by how these vortices collide, reconnect and separate. Very little is known directly about these microscopic interactions, even though macroscopic tangles have been generated, then observed to decay, in numerous experiments in ^{3}He or ^{4}He superfluids. Tangles that can be formed by counter-flow, towed grids, oscillating and vibrating grids in stationary superfluids, and collisions of vortex rings attached to ions (Skrbek & Sreenivasan 2012).

Theoretically, the observed decay can be explained if vortex reconnection can efficiently

convert the quantum kinetic energy associated with the vortices into the interaction energy of the system or into quantum waves. This would hold even for low temperature quantum fluids, including Bose-Einstein condensates, and in which the decay has been observed (Walmsley & Golov 2008). Systems without a quasi-classical normal fluid component, and therefore without a viscous mechanism to remove kinetic energy from the quantum vortices. Despite this, most of our current theoretical insight into quantum vortex reconnection has been through Lagrangian simulations of quantised vortex filaments that obey a form of the law of Biot-Savart and do not include the terms for the interaction energy. Why?

Part of the reason is that the Lagrangian approach has experimental support, most recently by comparisons between experiments tracking quantum vortices with solid hydrogen particles (Bewley *et al.* 2008; Paoletti *et al.* 2008) and the scaling in the filament calculation of initially anti-parallel vortices by de Waele & Aarts (1994). In both cases, the separation of the vortices was consistent with local dimensional analysis. That is if $\frac{d}{dt}\delta \sim v \sim \Gamma/\delta$, then one would expect that

$$\delta(t) \sim (\Gamma|t_r - t|)^{1/2}. \qquad (1.1)$$

This will be called the *dimensional scaling*.

Alternatively, one can simulate the underlying mean-field equations of quantum fluids and visualise vortex reconnection by following the low density isosurfaces that surround the zero density cores. The problem with this approach is that tracking the motion of the vortices within these isosurfaces is difficult, even for single interactions.

The aim of this paper is to begin to fill that gap using two innovations in the analysis of the mean-field equations. One innovation is in the initial conditions and the other innovation is for the analysis of the vortices. Together these allow us to track the motion of the reconnecting quantum vortices and determine scaling laws for two classes of initial configurations, orthogonal or anti-parallel vortices. Both simulated using the hard-sphere version of the Gross-Pitaevskii equations.

The conclusion will be that the scaling laws for the separations in the two configurations are distinctly different even when the pairs are several core radii apart. The anti-parallel case obeys the expectations from (1.1), but the orthogonal cases consistently obey a distinctly different type of scaling. These scaling differences will be associated with differences in the alignments of their respective Frenet-Serret coordinate frames that persist over all times.

This paper is organised as follows. First, the equations are introduced along with descriptions of the numerical model and initialisation of the anti-parallel and orthogonal vortex. This includes overviews of their global evolution in three-dimensions. Next, the methods used to identify the trajectories of the vortices and the local properties of the Frenet-Serret frame, including curvature. Next the results, arranged by the type of simulation, orthogonal then anti-parallel. Results include the time dependence of the separation of the vortices, the curvature along the vortices and alignments in terms of the Frenet-Serret frames. Finally, the differences between the two classes of initial conditions are discussed and how these differences might affect the observed scaling laws for the approach and release of reconnecting vortices.

2. Equations, numerics and initial condition

Following Berloff (2004), the three-dimensional Gross-Piteavskii equations used for simulating for the complex wave function or order-parameter ψ are

$$\frac{1}{i}\frac{\partial}{\partial t}\psi = E_v\nabla^2\psi + V(|\boldsymbol{x}-\boldsymbol{x}'|)\psi(1-|\psi|^2) \quad \text{with} \quad E_v = 0.5 \text{ and } V(|\boldsymbol{x}-\boldsymbol{x}'|) = 0.5\delta(\boldsymbol{x}-\boldsymbol{x}'). \tag{2.1}$$

These are the mean-field equations of a microscopic, quantum system with $\hbar$ and m non-dimensionalized to be 1, a chemical potential of $E_v = 0.5$ and using the hard-sphere approximation for $V(|\boldsymbol{x}-\boldsymbol{x}'|)$. They are an example of a defocusing nonlinear Schrödinger equation. All calculations in this paper will use (2.1).

These equations conserve mass:

$$M = \int dV |\psi|^2 \tag{2.2}$$

and a Hamiltonian

$$H = \tfrac{1}{2}\int dV \left[\nabla\psi \cdot \nabla\psi^\dagger + 0.25(1-|\psi|^2)^2\right] \tag{2.3}$$

where $\psi^\dagger$ is the complex conjugate of ψ. It is often useful to define

$$K_{\nabla\psi} = \tfrac{1}{2}|\nabla\psi|^2 \quad \text{and} \quad I(\boldsymbol{x}) = \tfrac{1}{4}(1-|\psi|^2)^2 \tag{2.4}$$

where $K_{\nabla\psi}$ is the kinetic or gradient energy and I is the interaction energy.

Unlike the incompressible Navier-Stokes equations, these equations are a Hamiltonian system conserve their global energy, and are known to be regular (without finite-time singularities) for all times. Due to the reflective/Neumann boundary conditions on the domain, the net momentum over computed domain can change. However, over the periodic domain that the computational domain is embedded within, the net momentum is identically zero and therefore conserved for all times. Isosurfaces of $K_{\nabla\psi}$ are including in Figs. 2.1, 2.2, 2.3, 4.3 and 5.1, for future reference.

Several important properties of quantum vortex reconnection have been previously demonstrated by the Gross-Pitaevskii calculations. First, it has been demonstrated (Leadbeater *et al.* 2003; Berloff 2004; Kerr 2011) that the line length grows just prior to reconnection, indicating a type of vortex stretching. Second, reconnection radiates energy. Either as sound waves (Berloff 2004; Leadbeater *et al.* 2001, 2003), non-linear refraction waves (Berloff 2004; Zuccher *et al.* 2012) or strongly non-linear vortex rings (Leadbeater *et al.* 2003; Berloff 2004; Kerr 2011). About 10% of the initial kinetic energy $K_{\nabla\psi}$ is lost by these means during the initial reconnection (Kerr 2011). With added terms representing assumptions about the type of energy depletion at small-scales, these equations can also give us hints to why the vortex tangle decays (Sasa *et al.* 2011).

But can the Gross-Pitaevskii equations provide us with details about the reconnection processes underlying the tangle dynamics?

2.1. *Quasi-classical approximations*

At first glance, a continuum equation like (2.1) does not appear to be a useful tool for studying the Lagrangion motion of vortex lines in three-dimensional space. However, by writing the wave function as $\psi = \sqrt{\rho}e^{i\phi}$, where ρ is the density and ϕ s the complex phase, and using analogies with classical fluids, these equations do contain moving, time-dependent quantum vortices.

To see this, define the phase velocity $\boldsymbol{v}_\phi$ and the quanta of circulation Γ around the

line defects as

$$\boldsymbol{v}_\phi = \nabla\phi = \mathrm{Im}(\psi^\dagger \nabla\psi)/\rho \qquad \Gamma = \int \boldsymbol{v}_\phi \cdot \boldsymbol{s} = 2\pi \qquad (2.5)$$

then identify the $\rho \equiv 0$ line defects as quantum vortices by defining their dimensionless quantised circulation as $\Gamma = \oint \boldsymbol{v} \cdot d\boldsymbol{s} = 2\pi$. Even though they lack a true vorticity field because $\nabla \times \boldsymbol{v}_\phi = \nabla \times \nabla \cdot \phi \equiv 0$. In this picture, vortex reconnection appears naturally as the instantaneous re-alignment of these lines and exchange of circulation when the line defects meet. If dimensions were added, the quantised circulation has the classical units of circulation: $\Gamma \sim \rho L^2/T$. Note these differences with classical vortices governed by the Navier-Stokes equation: Classical circulation is not quantised and viscous reconnection is never 100%.

To extract the Lagrangian motion of quantum vortices from fields defined on three-dimensional meshes these issues must be addressed:

• First, the solution should not be dominated by linear waves and there should not be strong fluctuations along the vortex trajectories.

• Second, a method is needed for identifying the direction and positions that the vortices follow as they pass through the three-dimensional mesh.

Due to these issues, most numerical work on macroscopic quantum tangles still use Lagrangian algorithms (Barenghi 2008). The two innovations introduced in this paper resolve both problems and then allow us to extract smooth motion for the vortices from the calculated solutions of the Gross-Pitaevskii equations on Eulerian meshes.

To complete the discussion of the Gross-Pitaevskii equations (2.1), the full analogy to classical hydrodynamic equations comes from inserting $\psi = \sqrt{\rho}\exp(i\phi)$ into (2.1) to get the standard equation for ρ and a Bernoulli equation for ϕ:

$$\frac{\partial}{\partial t}\rho + \nabla \cdot (\rho \boldsymbol{v}_\phi) = 0 \qquad \frac{\partial}{\partial t}\phi + (\nabla\phi)^2 = 0.5(1-\rho) + \nabla^2\sqrt{\rho}/\sqrt{\rho}. \qquad (2.6)$$

The $\boldsymbol{v}_\phi$ velocity equation can then be formed by taking the gradient of the ϕ equation.

As previously described (Kerr 2011), the numerics are a standard semi-implicit spectral algorithm where the nonlinear terms are calculated in physical space, then transformed to Fourier space to calculate the linear terms. In Fourier space, the linear part of the complex equation is solved through integrating factors with the Fourier transformed nonlinearity added as a 3rd-order Runge-Kutta explicit forcing. The domain is imposed by using no-stress cosine transforms in all three directions. For all of the calculations the domain size is $L_x \times L_y \times L_z = (16\pi)^3 \approx 50^3$ or $(32\pi)^3$. Both 128^3 and 256^3 grids were used, with the 256^3 grid giving smoother temporal evolution.

2.2. *Choice of initial configurations and profiles*

Configurations. Two initial vortex configurations are used in this paper, anti-parallel vortices with a perturbation, and orthogonal vortices. Both configurations have been used many times for both classical (Navier-Stokes) and quantum fluids, including the first calculations using the three-dimensional Gross-Pitaevskii equations (Koplik & Levine 1993).

The advantage of focusing on these configurations is that the initial reconnection for most other configurations, for example colliding or initially linked, vortex rings, can be reduced to either anti-parallel or orthogonal dynamics, for which less global resolution is needed to resolve the reconnection. This is because the initial reconnection events require, effectively, only half of each ring.

These two configurations also represent the two extremes for the initial chirality or linking number of the vortex lines in a quantum fluid. In classical cases (Boratav *et al.*

$\rho = .05, \max(\text{KE}) = 0.83, \max|\omega| = .4$

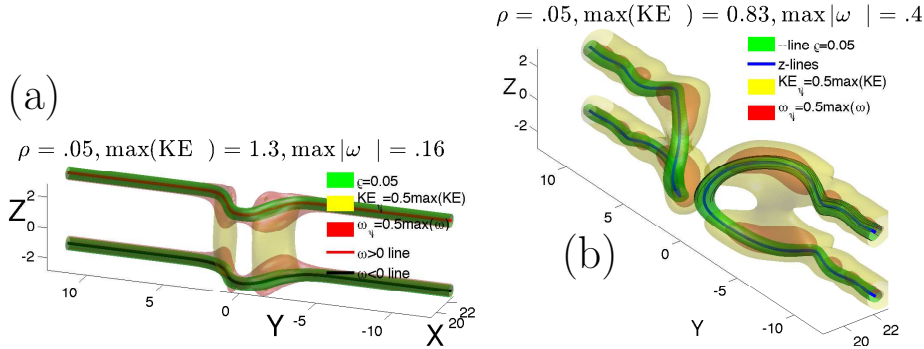$\rho = .05, \max(\text{KE}) = 1.3, \max|\omega| = .16$

FIGURE 2.1. Anti-parallel case: Density, kinetic energy $K_{\nabla\psi} = |\nabla\psi|^2$ and pseudo-vorticity $|\nabla\psi_r \times \nabla\psi_i|$ isosurfaces plus vortex lines at these times: (a) $t = 0.125$, with $\max(K_{\nabla\psi}) = 1.3$, and (b) $t = 4$ with $\max(K_{\nabla\psi}) = 0.83$. $\max|\omega_\psi| = 0.4$ for all the times. The vortex lines show that the pseudo-vorticity method not only follows the lines $\rho = 0$ well, but the $t = 4$ frame also shows that it can be used to follow isosurfaces of fixed ρ. The $t = 0.125$ frame shows that initially the kinetic energy is largest between the elbows of the two vortices, with large ω_ψ at the elbows. The $t = 4$ frame shows the newly reconnected vortices as they are separating with undulations on the vortex lines that will form additional reconnections and vortex rings at later times.

1992).this is determined by the global helicity, the integral of the scalar product of the vorticity and velocity: $h = \int (\nabla \times \boldsymbol{u}) \cdot \boldsymbol{u} dV$. The global helicity h is a quadratic invariant of the three-dimensional incompressible Euler equations in addition to the kinetic energy. There is a similar helicity in magnetohydrodynamics and in both cases the presence of helicity tends to suppress nonlinear interactions. The converse holds for anti-parallel cases, whose net helicity is zero, has the strongest initial instabilities.

Density profile. The density profiles for all the vortex cores in this paper are determined by the following Padé approximate:

$$|\psi_{sb}| = \sqrt{\rho_{sb}} = \frac{c_1 r^2 + c_2 r^4}{1 + d_1 r^2 + d_2 r^4} \tag{2.7}$$

with $c_1 = 0.3437$, $c_2 = 0.0286$, $d_1 = 0.3333$, and $d_2 = 0.02864$.

Note that $c_2 \lesssim d_2$, which implies that as $r \to \infty$, the density approaches the usual background of $\rho = 1$ from below more slowly than in the true Padé of this order that was derived by Berloff (2004) with $c_2 = d_2 = 0.02864$. Therefore, the profile with $c_2 \lesssim d_2$ is designated as ψ_{sb} because it is a sub-Berloff (2004) profile. Furthermore, because the calculations are in finite domains, to ensure that the Neumann boundary conditions are met, a set of up to 24 mirror images of the vortices are multiplied together. This multiplication process takes the slight original $r \to \infty$, $\rho_{sb} < 1$ differences and generates even stronger differences at the boundaries with $(1 - \rho) \approx 0.02 - 0.03$.

For all of the configurations discussed here, using this $|\psi| \lesssim 1$ initial profile appears to be crucial in allowing us to obtain clear scaling laws for the pre- and post-reconnection separation of the vortices. As discussed in Section 4, the temporal separations of all of the true Padé approximates had significant fluctuations.

Once the best profile has been chosen, then one must choose the trajectories of the interacting vortices. The anti-parallel initial trajectories are covered first because the three-dimensional images show all the three-dimensional diagostics to be used.
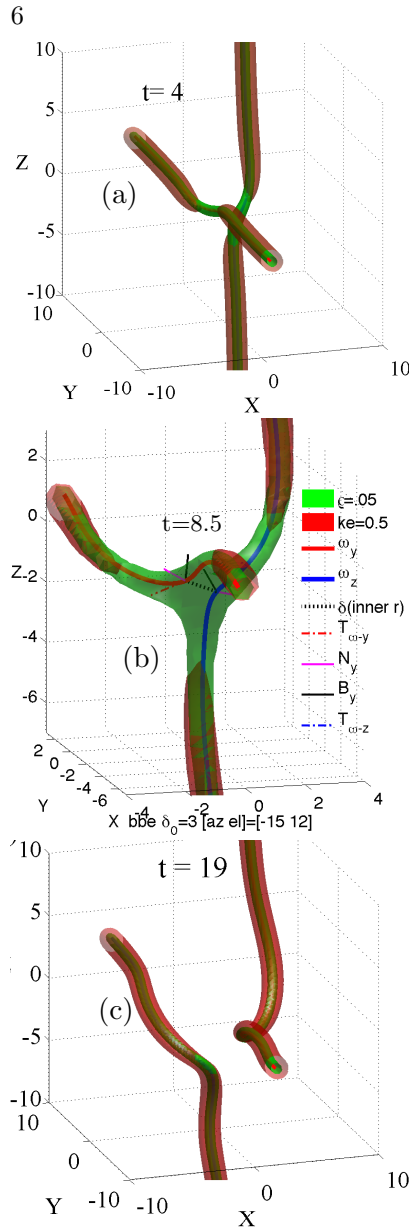
FIGURE 2.2. Overview of the development for the $\delta_0 = 3$ 128^3 orthogonal calculation from a general 3D perspective for three times, one at $t = 4$, just before reconnection at $t = 8.5$, where $t_r \approx 8.92$ for 256^3 resolution, and one at $t = 19$, after reconnection. The centres of the vortices (red and blue) are given in each case, but the Frenet-Serret frames are given only for $t = 8.5$ and are presented better for $t = 8.75$ in figure 4.3. Brown (red+green) isosurfaces of strong K_ψ encase the green low density $\rho = 0.05$ isosurfaces only at the ends of the vortices for $t < t_r$ and encase all along the vortices at $t = 19 >> t_r$. Because the momentum is so small (that is only the $\rho = 0.05$ green appears) around the reconnection, this suggests that the dynamics driving the vortices together during the final stages of reconnection is controlled by the cubic nonlinearity in (2.1) rather than the Laplacian term, which contains the phase velocity. Post-reconnection, from this perspective, a twist in the right-hand vortex can be seen.
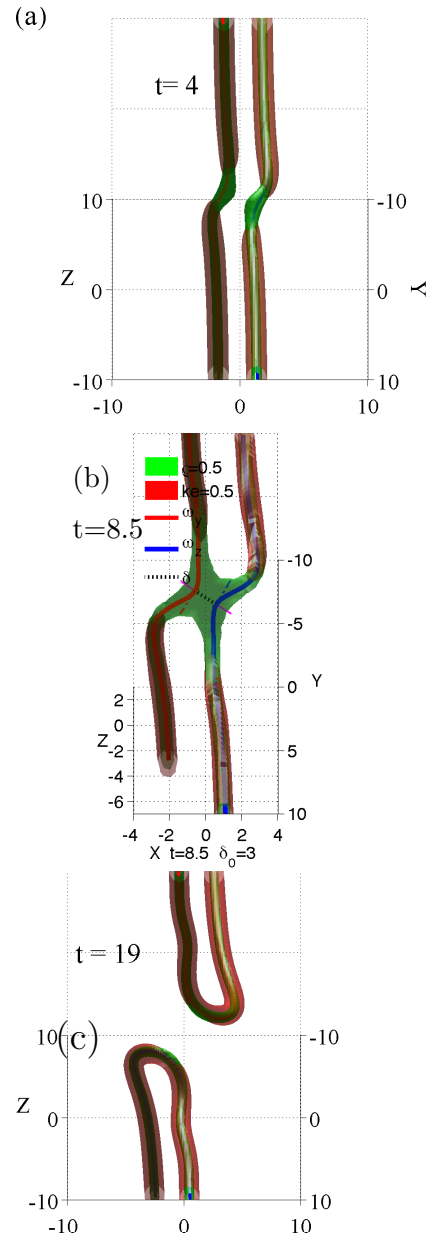

FIGURE 2.3. The same $\delta_0 = 3$ fields and times as in Fig. 2.2 from the Nazarenko perspective, which looks down the $45°$ *propagation plane* in the $y-z$-plane in Fig. 4.5. This projection is useful because the pre- and post-reconnection symmetries can be seen most clearly, which is why it is the basis for comparison of reconnection angles in Fig. 4.6 and Section 4.5. The arms are extending away from the *reconnection plane*, either towards or away from the viewer, Also note that from this perspective, loops are clearly not forming.

type		δ_0	t_r	$K_{\nabla\psi}(t=0)$	I_0
$\perp$ 256^3		2	2.7	0.0074	0.0023
$\perp$ 128^3		3	9.7	0.0074	0.0023
$\perp$ 256^3		3	9	0.0074	0.0023
$\perp$ 256^3		4	21	0.0074	0.0023
$\perp$ 256^3		5	40	0.0074	0.0023
$\perp$ 256^3		6	68	0.0074	0.0023
$\parallel$ 256^3		4	2.44	0.0056	0.0031

TABLE 1. Cases: Type is orthogonal $\perp$ or anti-parallel $\parallel$, initial separations, approximate reconnection times, initial kinetic and interaction energies.

2.3. *Anti-parallel: Initial trajectory and global development.*

Based upon past experience with anti-parallel classical vortices, Kerr (2011) chose the perturbations of the trajectories of the quantum vortices to be in their direction of propagation with their path and profile defined by:

1) The perturbation of the trajectory was localised with the following analytic function.

$$ \boldsymbol{s} = \left(\delta_x \frac{2}{\cosh\big((y/\delta_y)^{1.8}\big)} - 1, 1, 0 \right) \tag{2.8} $$

with $\delta_x = -1.6$ and $\delta_y = 1.25$. The power 1.8 on the normalized position

2) The profiles were applied perpendicular to trajectory, and not perpendicular to just the y-axis, the primary direction of the vortices.

As in Kerr (2011), two of the Neumann boundaries acting as symmetry planes to increase the effective domain size. These planes are the $y = 0$, $x - z$ *perturbation plane* and $z = 0$, $x - y$ *dividing plane*. Because the goal of this calculation was to focus upon the scaling around the first reconnection, the long domain used in Kerr (2011) to generate a chain of vortices is unnecessary and L_y is less. One difference is that, based upon recent experience with Navier-Stokes reconnection (Kerr 2013a), L_z was increased to ensure that the evolving vortices do not see their mirror images across the upper z Neumann boundary condition.

Figure 2.1 shows the state at $t = 0.125$, essentially the initial condition, and the state at $t = 4$, after the first reconnection event at $t_r \approx 2.4$. Three isosurfaces are given. Low density isosurfaces ($\rho = 0.05$), isosurfaces of the kinetic energy $K_{\nabla\psi}$ (2.4) and isosurfaces of $|\boldsymbol{\omega}_\psi|$ (3.1), a pseudo-vorticity that is introduced in the next section. The vortex lines defined by $\boldsymbol{\omega}_\psi$ and Proposition 1 are shown using thickened curves. The structure at the time of reconnection is discussed in Section 5 using Figure 5.1 and how the flow would develop later has already been documented by Kerr (2011), which shows several reconnections forming a stack of vortex rings.

Both $K_{\nabla\psi}$ and $\boldsymbol{\omega}_\psi$ are functions of the first-derivatives of the wave function, but show different aspects of the flow. The $K_{\nabla\psi}$ isosurfaces indicate where momentum is large, with the $t = 0.125$ surfaces indicated that the initial forward motion is between the initial perturbations and the $t = 4$ post-reconnection $K_{\nabla\psi}$ surfaces showing that the primary motion is around the vortices. $|\boldsymbol{\omega}_\psi|$ is large where the vortex cores bulge and have the greatest curvature.

2.4. *Orthogonal: Initial separations and global development.*

The placement of the orthogonal vortices is relatively easy compared to specifying the anti-parallel trajectories. All that is needed is to choose two points in x on either side of $x = y = z = 0$ and have a line parallel to the y axis go through one of these points and a line parallel to the z axis go through the other. The five separations simulated are given in Table 1. Because all of the orthogonal cases with $\delta_0 \geq 2$ behave qualitatively in the same manner, all of the orthogonal three-dimensional images will be taken from the 128^3, $\delta_0 = 3$ calculation, whose estimated reconnection time is $t_r = 9.7$.

The first two sets of three-dimensional isosurfaces and vortex lines in Figs. 2.2 and 2.3 are used to show the global evolution of the vortices through reconnection, with Fig. 2.2 provides a true three-dimensional perspective of the orthogonality and Fig. 2.3, defined by Fig. 4.6, providing a perspective down the $y = z$ axis, which is also used for the determination of three-dimensional angles in subsection 4.3. The three times chosen for each are $t = 4$, pre-reconnection, $t = 8.5$ as reconnection begins, and $t = 19$, post-reconnection.

The two isosurfaces are for a low density of $\rho = 0.05$ and kinetic energy of $K_{\nabla\psi} = 0.5$, where $\max(K_{\nabla\psi}) = 0.58$. There are two pseudo-vortex lines (3.1) in each frame, one that originates on the $y = 0$ plane and the other on the $z = 0$ plane. The $t = 8.5$ frame also shows some additional orientation vectors that will be discussed in Section 4.

Qualitative features are:

• The initially orthogonal vortices are attracted towards each other at their points of closest approach, asymmetrically bending out towards each other.

• During this stage there is a some loss of the kinetic energy between $t = 8$ and $t = 11$, $\Delta K_{\nabla\psi} < 10\% K_{\nabla\psi}(t = 0)$. This is converted into interaction energy I (2.4). There are no further noticeable changes in $K_{\nabla\psi}$ for $t > 12$.

• After reconnection, from one perspective there is a slight twist on one vortex, but it is not twisted enough for the vortices to loop back upon themselves and reconnect again. Instead, the two new vortices pull back from one another and do not reconnect again, as shown by the $t = 19$ frame in figure 2.2. Consistent with experimental observations of vortex interactions using solid hydrogen particles (Bewley *et al.* 2008; Schwarzschild 2010) in the sense that post-reconnection filaments simply pull back from one another and do not loop.

• Two sketches of the alignments and an addition isosurface perspective are used in subsection 4.2 to illustrate this evolution further.

3. Approach and separation of vortex lines: Methodology

The primary result in this paper will be the differences in the temporal scaling of the pre- and post-reconnection separation of the vortices for the two configurations. The secondary results are clues for the origin of these differences in the evolution of the local curvature and Frenet-Serret frames on the vortices for the two configurations. To achieve this, one needs an initial condition for which the evolution of the vortices is smooth and a means to follow that evolution. The key ingredient of the initial condition is provided

by the choice of coefficients in (2.7). This section will show what is needed to accurately track the vortices. Two methods for detecting the vortices have been used.

3.1. *Detecting lines by finding $\rho = 0$ mesh cells.*

The first approach is to estimate the locations of the $\rho \equiv 0$ quantum vortex lines by extracting the positions of the vertices of a $\rho \gtrsim 0$ isosurface mesh, determined by Matlab, then average these positions. For this method to work, the density ρ has to be small enough so that there are only 3-6 points clustered in a plane perpendicular to the vortex lines. The method begins to fail around reconnection points because there is an extensive $\rho \approx 0$ zone as the cores of the vortices start to overlap, resulting in the isosurface points that are too far apart to make reliable estimates for the positions of the $\rho \equiv 0$ cores. Due to these problems, this approach is used only for providing the seeds for our preferred approach and its validation.

3.2. $\boldsymbol{\omega}_\psi = \nabla\rho \times \nabla\phi$ *pseudo-vorticity method*

The second approach begins by recognising that the line of zero density should be perpendicular to the gradients of the real and imaginary parts of the wave function. Therefore it is useful to define the following *pseudo-vorticity*:

$$\boldsymbol{\omega}_\psi = 0.5\nabla\psi_r \times \nabla\psi_i \tag{3.1}$$

The inspiration for this approach comes from how to write the vorticity in terms of a cross production of the scalars in Clebsch pairs, which is an alternative approach to representing the incompressible Euler equations.

PROPOSITION 1. *At points with $\rho = 0$, the direction of the quantum vortex line is defined by the direction of $\boldsymbol{\omega}_\psi = 0.5\nabla\psi_r \times \nabla\psi_i$.*

Proof. A quantum vortex line is defined by $\rho \equiv 0$, further $\rho = \psi_r^2 + \psi_i^2$ which together imply that $\psi_r = \psi_i = 0$ on this vortex line.

Then define $\hat{\omega}_\rho$ the direction vector of the line at any arbitary point on the vortex line. Clearly in this direction we see the value of ψ_r and ψ_i does not change and thus we observe that

$$\hat{\omega}_\rho \cdot \nabla\psi_r = \hat{\omega}_\rho \cdot \nabla\psi_i = 0$$

$\nabla\psi_i$ at these points. Thus this is only possible if $\hat{\boldsymbol{\omega}}_\rho = (\nabla\psi_r \times \nabla\psi_i)/|\nabla\psi_r \times \nabla\psi_i|$. $\quad\square$

By itself, this proposition does not tell us where the vortex lines lie because one still needs a method for identifying a point on the line. To find starting points for a streamline function, the first method is used to identify points on the boundaries where $\rho \approx 0$.

Potentially there could have been difficulties near the time and position of reconnection because both $\rho \approx 0$ and $\nabla\psi_{r,i}$ are small, perhaps too small for the identifying the positions of neigbouring lines with $\rho \approx 0$. In practice, this has not been a problem.

Once the lines have been found, the derivatives along their trajectories of their three-dimensional positions can be determined, and from those derivatives the local curvature, Frenet-Serret coordinate frames and possibly the local motion of the lines can be found. Properties that can be compared to the predictions of vortex filament models.

To analyse these properties, the following alternative definition of the pseudo-vorticity is useful.

COROLLARY 1. $\hat{\boldsymbol{\omega}}_\rho = \hat{\boldsymbol{\omega}}_\psi$ *where* $\hat{\boldsymbol{\omega}}_\rho = \nabla\rho \times \nabla\phi/|\nabla\rho \times \nabla\phi|$

Proof. Start with $\psi_r = \sqrt{\rho}\cos\phi$ and $\psi_i = \sqrt{\rho}\sin\phi$.

Expand: $0.5\nabla\psi_r \times \nabla\psi_i = [\nabla\sqrt{\rho}\cos\phi - \sqrt{\rho}\sin\phi\nabla\phi] \times [\nabla\sqrt{\rho}\sin\phi + \sqrt{\rho}\cos\phi\nabla\phi]$.
Remove all ψ_r and ψ_i terms sharing the same gradient to reduce this to

$$2(\nabla\sqrt{\rho} \times \nabla\phi\sqrt{\rho}\cos^2\phi - \nabla\phi \times \nabla\sqrt{\rho}\sqrt{\rho}\sin^2\phi)$$

Finally, use $\nabla\sqrt{\rho} = \nabla\rho/(2\sqrt{\rho})$ to get $\boldsymbol{\omega} = \nabla\rho \times \nabla\phi$.

$\square$

Do these lines follow the cores of $\rho \equiv 0$? One test is to interpolate the densities from the Cartesian mesh to the vortex lines. The result is that these densities are very small, but not exactly zero. Another test is simultaneously plot the pseudo-vorticity lines along with very low isosurfaces of density, examples of which is given in Fig. 2.1 and Fig. 2.2. The centres of the isosurfaces and the lines are almost indistinguishable.

The motion of the $\rho = 0$ lines can, in principle, be determined exactly using just the time derivatives of ψ_r and ψ_i, the real and imaginary parts of the wavefunction ψ and their gradients $\nabla\psi_r$ and $\nabla\psi_i$, can we construct the motion of the vortex lines from the following, which will will be used in a later paper.

PROPOSITION 2. *The motion of the vortex line is given by the coupled set of equations*

$$
\begin{aligned}
(\nabla\psi_r \times \nabla\psi_i) \cdot \frac{d}{dt}\boldsymbol{x}(s,t) &= 0 \\
-\nabla\psi_r \cdot \frac{d}{dt}\boldsymbol{x}(s,t) &= -0.5\Delta\psi_i \\
-\nabla\psi_i \cdot \frac{d}{dt}\boldsymbol{x}(s,t) &= 0.5\Delta\psi_r
\end{aligned}
$$

.

The solution of which is

$$\frac{d}{dt}\boldsymbol{x}(s,t) = -0.5\frac{\Delta\psi_i(\boldsymbol{\omega}_\psi \times \nabla\psi_i) + \Delta\psi_r(\boldsymbol{\omega}_\psi \times \nabla\psi_i)}{\boldsymbol{\omega}_\psi^2} \tag{3.2}$$

where pseudovorticity $\boldsymbol{\omega}_\psi := \nabla\psi_r \times \nabla\psi_i$

Proof. We already know that the trajectory of the vortex lines is defined by the pseudovorticity $\boldsymbol{\omega}_\psi = \nabla\psi_r \times \nabla\psi_i$ from proposition above.

Since the density remains zero along this line, the motion we are interested in is perpendicular to this direction.

On the $\rho = \psi_r^2 + \psi_i^2 \equiv 0$ lines the time derivatives of $\psi_{r,i}$ are:

$$\frac{\partial}{\partial t}\psi_r = -0.5\Delta\psi_i$$

$$\frac{\partial}{\partial t}\psi_i = 0.5\Delta\psi_r$$

Next we can Taylor expand to first order $\psi_{r,i}$ about the parameterised curve $\boldsymbol{x}(s,t)$.

$$\psi_r = (\nabla\psi_r)(\boldsymbol{x} - \boldsymbol{x}(s,t)) \quad \text{and} \quad \psi_i = (\nabla\psi_i)(\boldsymbol{x} - \boldsymbol{x}(s,t))$$

and their time-derivatives again to first order are

$$
\begin{aligned}
\frac{\partial}{\partial t}\psi_r &= (\nabla\frac{\partial}{\partial t}\psi_r)(\boldsymbol{x} - \boldsymbol{x}(s,t)) - \nabla\psi_r\frac{d}{dt}\boldsymbol{x}(s,t) \approx -\nabla\psi_r\frac{d}{dt}\boldsymbol{x}(s,t) \\
\frac{\partial}{\partial t}\psi_i &= (\nabla\frac{\partial}{\partial t}\psi_i)(\boldsymbol{x} - \boldsymbol{x}(s,t)) - \nabla\psi_i\frac{d}{dt}\boldsymbol{x}(s,t) \approx -\nabla\psi_i\frac{d}{dt}\boldsymbol{x}(s,t)
\end{aligned}
$$

Adding that the motion will be perpendicular to the vortex (i.e. the pseudovorticity $\nabla\psi_r \times \nabla\psi_i$) to equating the two time derivative equations one gets the three coupled equations needed.

$\square$

3.3. Curvature obtained from the ω_ψ lines

The curvature of the lines identified by the pseudo-vorticity algorithm will be found by applying the Frenet-Serret relations to derivatives of the trajectories $\boldsymbol{r}(s)$ of the vortex lines.

Definition 3.1 *The Frenet-Serret frame for any smooth curve $\boldsymbol{r}(s) : [0,1] \to \mathbb{R}^3$ for which, at each point $\boldsymbol{r}(s)$, there is the orthonormal triple of unit vectors $(\boldsymbol{T}, \boldsymbol{N}, \boldsymbol{B})$ where $\boldsymbol{T}(s)$ is the tangent, $\boldsymbol{N}(s)$ is the normal and $\boldsymbol{B}(s)$ is the binormal. The following relations between $(\boldsymbol{T}, \boldsymbol{N}, \boldsymbol{B})$ define the curvature κ and torsion τ.*

$$\boldsymbol{T}(s) = \partial_s \boldsymbol{r}(s) \tag{3.3a}$$

$$\partial_s \boldsymbol{T} = \kappa \boldsymbol{N} \tag{3.3b}$$

$$\partial_s \boldsymbol{N} = \tau \boldsymbol{B} - \kappa \boldsymbol{T} \tag{3.3c}$$

$$\partial_s \boldsymbol{B} = -\tau \boldsymbol{N} \tag{3.3d}$$

The numerical algorithm for calculating the curvature and normal uses the function *gradient* in Matlab twice. That is, first $\boldsymbol{r}_{,s}$ and then $\boldsymbol{r}_{,ss}$ are generated. Next, normalising $\boldsymbol{r}_{,s}$ gives the tangent vector $\boldsymbol{T}$, the direction vector between points on the vortex lines. Finally, by manipulation of the derivative of $\boldsymbol{T}$, normalised, one gets $\boldsymbol{N}$, and the curvature from functions of $\boldsymbol{r}_{,s}$ and $\boldsymbol{r}_{,ss}$. The curvature formula is:

$$\kappa = |\boldsymbol{r}_{,s} \times \boldsymbol{r}_{,ss}| / |\boldsymbol{r}_{,s}|^3 \tag{3.4}$$

4. Orthogonal reconnection: New scaling laws and their geometry

The goals of this section are to to apply the pseudo-vorticity algorithm (3.1) to the evolution of the initially orthogonal vortex lines and use these positions to demonstrate that the separation scaling laws for the originally orthogal vortices deviate strongly from the mean-field prediction for all initial separations and for all times.

The major points to be demonstrated for the orthogonal calculations are:

• For strictly orthogonal initial vortices, there is just one reconnection and loops do not form out of the post-reconnection vortices in Fig. 2.2.

• The sub-Berloff profiles are crucial for obtaining temporal evolution that is smooth enough to allow clear scaling laws for the pre- and post-reconnection separtations to be determined (Rorai 2012).

• The separation scaling laws before and after reconnection are the same for each case, with these surprising results. Before reconnection $\delta_{in} \sim (t_r - t)^{1/3}$, which is slower than the dimensional scaling (1.1). And after reconnection $\delta_{in} \sim (t_r - t)^{2/3}$, faster than the dimensional scaling (1.1).

• This non-dimensional scaling arises as soon as the vortices adopt Frenet-Serret frames at their closest points whose vorticity tangent vectors are becoming anti-parallel and whose average tangent, curvature and bi-normal vectors with respect to the separation vector are: orthogonal, parallel and orthogonal.

• Reconnection occurs in the *reconnection or osculating plane* defined by the vorticity and curvature vectors at $t = t_r$ and is approximately the plane defined by the average
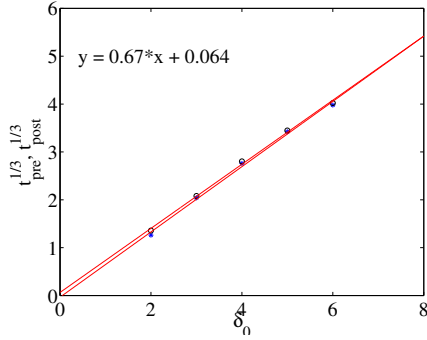
FIGURE 4.1. Reconnection times as a function of the initial separation. Reconnection times are estimated by using times immediately before and after reconnection plus the empirical 1/3 and 2/3 scaling laws.

vorticity and curvature vectors of the two vortices at points of closest approach for all times.

• Angles taken between the reconnection event and the larger scale structure are convex, not concave or acute, which could be the source of the non-dimensional separation scaling laws.

4.1. *Approach and separation*

The steps used to determine the separation scaling laws are these:

• First, identify the trajectories of the vortex lines with the pseudo-vorticity plus Matlab streamline algorithm. At any given time, both before and after reconnection:

○ The vortex originating on the $y = 0$ plane will be the y-vortex.

○ The vortex originating on the $z = 0$ plane will be the z-vortex.

• Identify the points, $\boldsymbol{x}_y$ and $\boldsymbol{x}_z$, of minimum separation between the two vortex lines, defined as $\delta_{yz}(t) = |\boldsymbol{x}_y - \boldsymbol{x}_z|$

○ and identify approximate reconnection times $\tilde{t}_r(\delta_0)$ when $\delta_{yz}(t)$ was minimal.

○ This generates δ_{yz} versus $t - t_r$ curves such as those in the inset of Fig.4.2.

• Once it was clear that neither the incoming nor outgoing separations obeyed the dimensional expectation (1.1), several alternative scaling laws were applied to the separations, with only the 1/3 incoming power law and outgoing 2/3 law working well for every case.

• These scaling laws are used to refine the approximate reconnection times $\tilde{t}_r(\delta_0)$ to give new $t_r(\delta_0)$. Then using the new t_r, make these two estimates:

○ Take the cube of the separations between the vortices over the last few time saves before the reconnection.

○ Take the outgoing separations to the 3/2 power for the first few time saves after the reconnection.

• The combined results give the fit $t_r = (0.67\delta_0 + 0.064)^3$ and are shown in Fig. 4.1.

• Then all of the separations were either cubed or taken to the 3/2 power and plotted with respect to their estimated reconnection times in Fig. 4.2 to show:

○ For all 5 cases and for all times:

○ $\delta_{in} \sim |t_r - t|^{1/3}$ for $t < t_r(\delta_0)$ and $\delta_{out} \sim |t - t_r|^{2/3}$ for $t > t_r(\delta_0)$.

○ The inset uses the dimensional scaling δ_{yz}^2 versus time to illustrate the differences between the new scaling laws and the dimensional prediction.

○ These results were first presented in Rorai (2012).

Sub-Berloff profile. Was it necessary to use the sub-Berloff profile? That is, could a different profile give similar separation collapse for all the δ_0 cases and obtain clear scaling laws, as in Fig. 4.2? To show the benefits of the sub-Berloff profile, tests were done using all of the known Padé approximate profiles of steady-state two-dimensional quantum
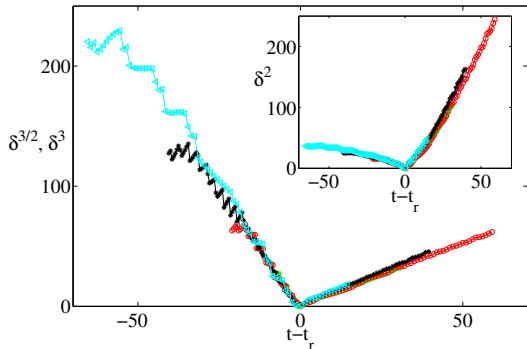
FIGURE 4.2. Pre- and post-reconnection separations for four cases: $\delta_0 = 3, 4, 5, 6$ for calculations with 256^3 points. $+$: $\delta_0 = 3$, $\bigcirc$: $\delta_0 = 4$, $*$: $\delta_0 = 5$, $\triangle$: $\delta_0 = 6$. Pre-reconnection distances are raised to the power 3, while post-reconnection distances are raised to the power 3/2. This scaling is visibly better than the dimensional prediction (δ^2 versus time to reconnection) shown in the inset. The scaled separations for $t < t_r$ fluctuate more strongly than the $t > t_r$ scaled separations.

vortices in an infinite domain, including tests with and without adding the mirror images. This included, the true Berloff profile, that is (2.7) with $c_2 = d_2 = 0.02864$, the low-order 2×2 Padé approximate of the Fetter (1969), (2.7) with $d_1 = 1$ and $c_2 = d_2 = 0$, and a variety 3×3 approximates from Berloff (2004) and most recently Rorai *et al.* (2012), solutions that are very close to the ideal diffusive solution. All gave roughly the same oscillations in the approach and separation curves as in Zuccher *et al.* (2012) and only a hint of the clear scaling laws in Fig. 4.2. Only the sub-Berloff profile with at least some of the mirror images worked.

Using $c_2 \lesssim d_2$ was discovered by chance and we do not have a clear explanation for why it works.

4.2. *Evolution of the orthogonal geometry during reconnection*

The evolution fo the three-dimensional structure is illustrated with the help of two sketches in figures 4.5 and 4.6 and the perspectives in figures 2.2, 2.3 and 4.3. The goal is to emphasize the differences with the anti-parallel case, give us some clues for why the separation laws are different and provide the reader with a mental picture of the evolution a system that is skew-symmetric and harder to visualise than the anti-parallel case with its planar symmetries. This initial discussion is divided into three parts. First, the choice of three-dimensional images. Second, the role of the sketches. Third, how to use your fingers to put the pieces together into a mental picture.

Choice of 3D images. Figures 2.2 and 2.3 use three times and two perspectives to illustrate the global changes in structure, as discussed in section 2.2. Figure 4.3 has been added to illustrate, over the period of reconnection, the details of the Frenet-Serret frames at the points of closest approach that are discussed in subsections 4.3 and 4.4. Only the zone around the reconnection point $\boldsymbol{x}_r$ is shown. The times are taken just as reconnection is beginning at $t = 6$, $t = 8.95$ just before the reconnection time of $t_r \approx 8.92$ and $t = 12$ as reconnection is ending. These frames show that the $\rho = 0.05$ isosurface changes slowly over the period from when the $\rho = 0.05$ surfaces of the vortices first meet until they separate while the $\rho \equiv 0$ pseudo-vorticity lines move rapidly towards one another.

Sketches: 2D and 3D. Figures 4.5 and 4.6 provide two planar sketches at or near the reconnection time of projections, with the best reference point for each being the mid-point between the closest points on the two vortices:

$$\boldsymbol{x}_r(\delta_0, t) = 0.5(\boldsymbol{x}_y(t) + \boldsymbol{x}_z(t)). \qquad (4.1)$$

The sketch in figure 4.5 projects the vortices at the reconnection time t_r onto the $y - z$ plane around the point of reconnection: $\boldsymbol{x}_r(\delta_0, t_r)$, along with projections of two planes of interest, the *reconnection or osculating plane* and the *propagation/symmetry plane*, which
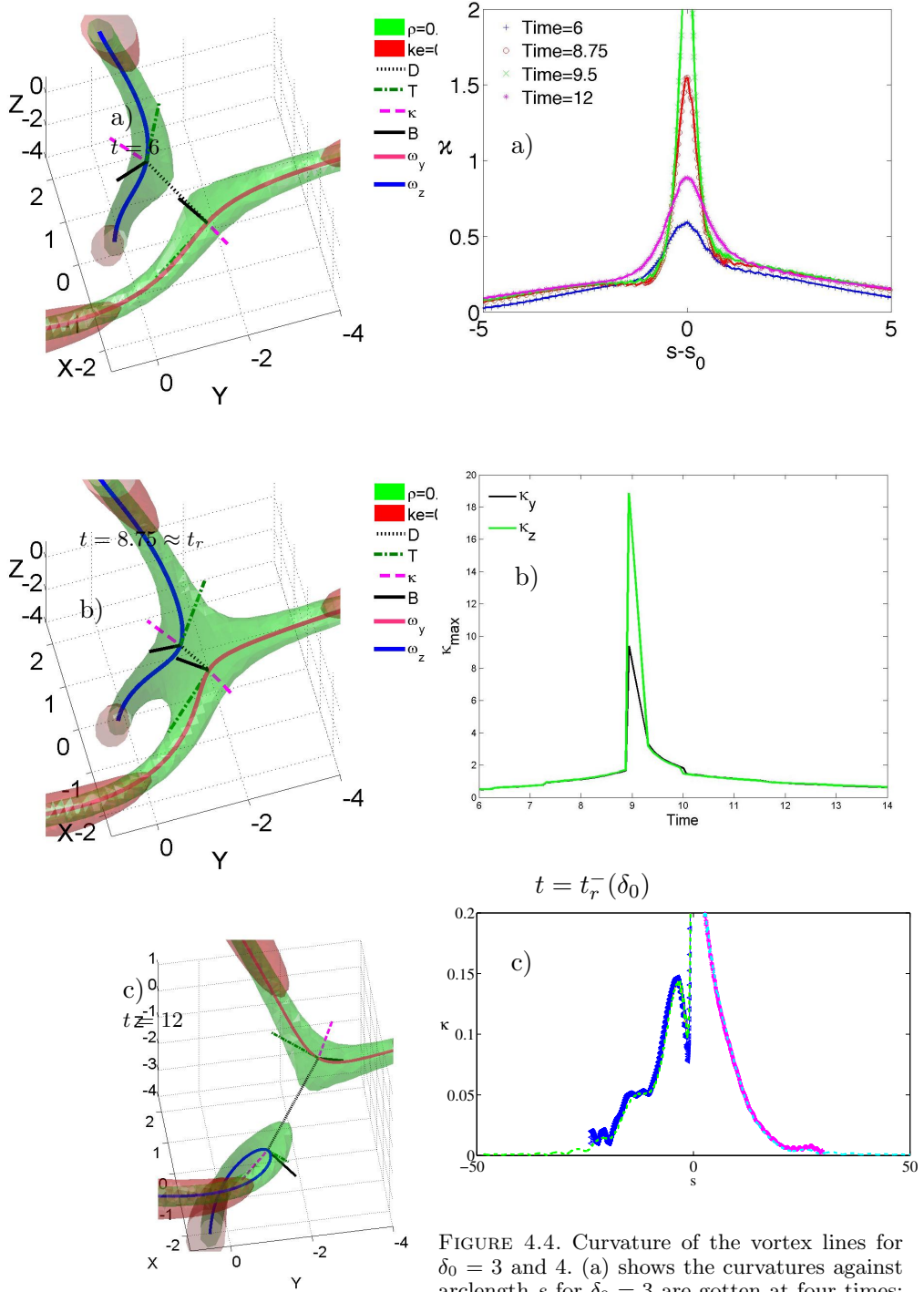
FIGURE 4.3. Isosurfaces, quantum vortex lines and orientation vectors in three-dimensions for the $\delta_0 = 3$, 128^3 calculation at $t = 6$ (4.3a), $t = 8.75$ (4.3b) and $t = 12$ (4.3c) where $t_r \approx 8.75$. Lines and vectors (separation and Frenet-Serret frames at the closest points on each vortex) are the same as in the $t = 8.5$ frame in Fig. 2.2.

FIGURE 4.4. Curvature of the vortex lines for $\delta_0 = 3$ and 4. (a) shows the curvatures against arclength s for $\delta_0 = 3$ are gotten at four times: $t = 6$, 8.75, 9.5 and 12. The curvature profiles of the two lines are nearly identical, so only one is shown. (b) shows the maximum curvatures of the two lines. Except around the reconnection time, the maxima of the two lines are nearly the same. (c) compares the pre-reconnection curvatures for $\delta_0 = 4$ for two domain sizes: $(16\pi)^3$ (blue-magenta) and $(32\pi)^3$ (green-cyan). Profiles are nearly identical except far from $s = s_0 = 0$.
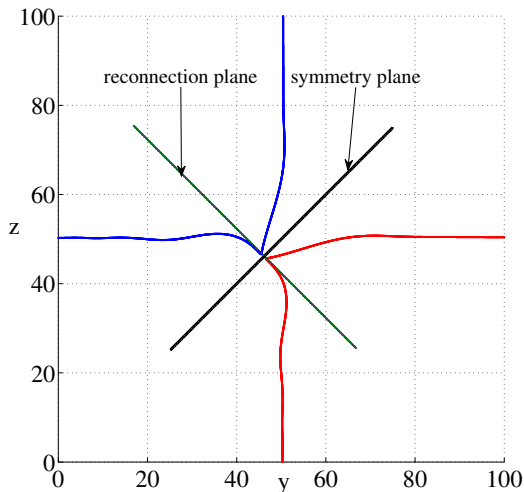
FIGURE 4.5. Sketch of the orthogonal reconnection around the reconnection point $\mathbf{x}_r$ at the reconnection time t_r of the vortices projected onto the $y - z$ plane. The pre-reconnection trajectories approximately follow the $y - y_{mid} = 0$ and $z - y_{mid} = 0$ axes and the post-reconnection trajectories are the red and blue lines. Two projected planes are indicated in black. The *reconnection plane* $(z - z_r) = -(y - y_r)$ that contains the tangents to the vortex lines $\boldsymbol{T}_{y,z}$ and their curvature vectors $\boldsymbol{N}_{y,z}$ both before and after reconnection, as well at the separation vector between the closest points $\boldsymbol{x}_{y,z}$. The *propagation/symmetry plane* $(z - z_r) = (y - y_r)$ which contains the bi-normals $\boldsymbol{B}_{y,z}$ and the *direction of propagation* of the mid-point $\boldsymbol{x}_r(t)$ between the closest points of the vortices: $\boldsymbol{x}_y$ and $\boldsymbol{x}_z$. From this perspective the angles along the *reconnection plane* before reconnection are shallow, and those after reconnection are sharp.
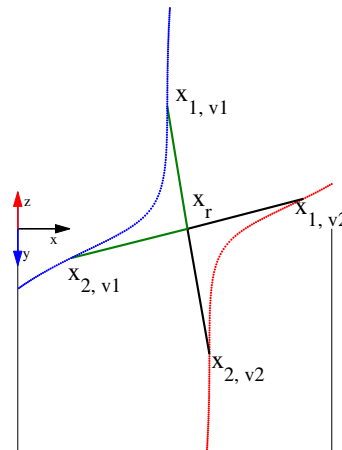

FIGURE 4.6. Sketch using the Nazarenko projection, that is looking down on the *reconnection plane* along the *propagation/symmetry plane*, just before reconnection. Four line segments (in three-dimensions) have been added that connect $\boldsymbol{x}_r$, the mid–point between the vortices at closest approach, to four points, each located Δs units along the vortices from their respective closest points. Angles generated between adjacent segments as a function of Δs are plotted in figure 4.10.

are defined in terms of the average Frenet-Serret basis vectors (4.2) in subsection 4.4. The second sketch in Fig. 4.6 looks down the $x = 0$, $y = z$ 45° *direction of propagation* of $\boldsymbol{x}_r(\delta_0, t)$ onto the $\boldsymbol{T}_{av} \times \boldsymbol{N}_{av}$ (4.2) *reconnection plane*. Important features include:

• Because Fig. 4.5 is at $t = t_r$, the projections of the planes and vortices all cross at $\boldsymbol{x} = \boldsymbol{x}_r(\delta_0, t_r)$, which means that the red and blue curves trace both the pre- and post-reconnection trajectories of the vortices, as follows:

○ The trajectories before reconnection follow the curves parallel to the $y = 0$ and $z = 0$ axes that are half blue and half red. These are projections of the red and blue lines in Fig. 4.6.

○ The trajectories immediately after reconnection are indicated by the red and blue curves coming out of the *reconnection plane*.

• The two orthogonal lines through $\boldsymbol{x}_r$ represent two planes:

○ The *reconnection plane*, defined by $\boldsymbol{T}_{av} = 0.5(\boldsymbol{T}_y - \boldsymbol{T}_z)$ and $\boldsymbol{N}_{av} = 0.5(\boldsymbol{N}_y - \boldsymbol{N}_z)$ (4.2). Before or after reconnection, the separation vector $\boldsymbol{D} = (\boldsymbol{x}_z - \boldsymbol{x}_y)/|\boldsymbol{x}_z - \boldsymbol{x}_y| \neq 0$ is also in this plane.

—— It is shown below that $\boldsymbol{T}_{y,z}$ and $\boldsymbol{N}_{y,z}$ swap at reconnection, so all of these basis vectors stay in this plane after reconnection.

    ◦ And the *propagation plane*, which contains the velocity of $\boldsymbol{x}_r(\delta_0, t)$ and the average bi-normal $\boldsymbol{B}_{av} = 0.5(\boldsymbol{B}_y + \boldsymbol{B}_z)$ (4.2).

• The $x = 0$, $y = z$ projection in Fig. 4.6 is denoted the Nazarenko projection or NP because it was used by linear model of Nazarenko & West (2003).

    ◦ That model tells us that $\boldsymbol{x}_r = 0.5(\boldsymbol{x}_y + \boldsymbol{x}_z)$ translates in the $(-y, -z)$ direction, motion that implies that the reconnection does not occur at the centre of the computational box.

    ◦ Note that for the points on either side of $\boldsymbol{x}_r$, the tangents $\boldsymbol{T}_{y,z}$ and curvature vectors $\boldsymbol{N}_{y,z}$ are anti-parallel. The components that are not anti-parallel are out of the NP projection. This also holds for the lines across the central, green $\rho = 0.05$ isosurface in Fig. 4.3b. Fig. 4.7a shows how $\boldsymbol{T}_y \cdot \boldsymbol{T}_z$, $\boldsymbol{N}_y \cdot \boldsymbol{N}_z$ and $\boldsymbol{B}_y \cdot \boldsymbol{B}_z$ converge to this state as $t \to t_r$.

    ◦ The lines drawn across the centre of Fig. 4.6 are used to determine long-range angles discussed in Section 4.5.

• **3D by using fingers.** Now cross your index fingers at the second knuckles so that they are pointing at $45°$ angles to the vertical.

    ◦ This is the same as rotating Fig. 4.5 by -135° so that the kink to the south-west is pointing north.

    ◦ Separate your fingers slightly.

    ◦ Now move your fingers up, bending them as you do and bringing the second knuckles together.

    ◦ This is how, the alignments of the Frenet-Serret frames at the points of closest approach (the second knuckles) in Fig. 4.7 form.

    ◦ Now hold that configuration and rotate it to get the configurations of the sketches in Figs. 4.5,4.6 and the three-dimensional images in Fig. 2.2b, 2.3b and 4.3b.

4.3. *Curvature*

Curvature, has played a central role in the history of quantum turbulence through its role in predicting the velocities of the quantum vortices in the law of Biot-Savart and the local induction approximation. The connection between these approximations for the velocities and the true dynamics of quantum fluids, as modeled by the Gross-Pitaevskii equations, would be in how the phase of the wavefunction is modified by the curvature of the vortex lines, and from that now the phase velocity is modified.

In that context, could curvature profiles provide clues for the origins of the anomalous scaling exponents of the orthogonal separations? To assess any possible role for κ in generating the new orthogonal vortex scaling laws, profiles of the curvature κ were determined using gradients on the vortex lines (3.4) for the $\delta_0 = 3$, 256^3 calculation for $6 \leq t \leq 12$, as shown in figure 4.4.

Figure 4.4a shows the curvatures of only one of the two vortices because their profiles were nearly identical except for the sharp spikes in the point of closest approach. The only significant difference between the two is at the spikes with the curvature maxima near t_r shown in figure 4.4b. Figure 4.4c compares $\delta_0 = 4$ calculations in two domains: $\Delta s \approx 16\pi = 50$ and $\Delta s \approx 32\pi = 100$, where the centres of the lines are at $s = 0$.

That the profiles of the two vortices were the same both before and after was not expected. Before looking carefully at the data, it seemed possible that the difference between the pre- and post-reconnection scaling laws could be due to the slight asymmetries in the curvature profiles on either side of the points of closest approach and the possibility that the high curvature sides could reconnect with one another. Instead, a symmetry is maintained with the strong segments reconnecting to the weak segments from the other vortex.

Another possible explanation, if the local induction approximation is relevant, would be if the curvature maxima are stronger post-reconnection. The inset in figure 4.4 does show that the maxima are slightly stronger post-reconnection, but this does not appear to be the whole story. To get a bigger picture we need to look beyond the curvature profiles and see how the vortices are aligned with each other for points along their entire trajectories. Starting with the alignments of their respective Frenet-Serret frames at the points of closest approach, then for distances away from those points.

4.4. *Orthogonal: Frenet-Serret orientation.*

Besides allowing us to calculate the curvature of the vortex lines, knowing their trajectories allows us to calculate the Frenet-Serret frame (3.3). This has been done for the 128^3, $\delta_0 = 3$ calculation for all times and provides quantitative support for the describing the local frame at the reconnection point $\boldsymbol{x}_r$ in terms of the *reconnection plane* and the *propagation plane* indicated in Fig. 4.5.

Figures 4.7 and 4.8 show the following evolution of the Frenet-Serret frames at the closest points $\boldsymbol{x}_{y,z}$:

- For $t < t_r$, pre-reconnection:
  ○ Fig. 4.7a shows that the vorticity direction or tangent vectors $\boldsymbol{T}_{y,z}$, the curvature vectors $\boldsymbol{N}_{y,z}$ and the bi-normals $\boldsymbol{B}_{y,z}$ converge to their opposites as $t \to t_r$, both before and after reconnection.
  ○ Fig. 4.7b shows that $\boldsymbol{T}_{y,z}$, $\boldsymbol{N}_{y,z}$ and their unit separation vector $\boldsymbol{D} = (\boldsymbol{x}_z - \boldsymbol{x}_y)/|\boldsymbol{x}_z - \boldsymbol{x}_y|$ all lie in the same plane, the *reconnection plane* in Fig. 4.5.
  ○ The bi-normals $\boldsymbol{B}_{y,z}$ define the *propagation plane*.
  ○ The useful averages of the Frenet-Serret frames between $\boldsymbol{x}_y$ and $\boldsymbol{x}_z$ are these:

$$
\begin{aligned}
\circ \quad \boldsymbol{N}_{av} &= 0.5(\boldsymbol{N}_y - \boldsymbol{N}_z) && \text{and is parallel to } \boldsymbol{D}(t) \\
\circ \quad \boldsymbol{T}_{av} &= 0.5(\boldsymbol{T}_y - \boldsymbol{T}_z) && \text{and is perpendicular to both } \boldsymbol{N}_{av} \text{ and } \boldsymbol{D}. \\
\circ \quad \boldsymbol{B}_{av} &= 0.5(\boldsymbol{B}_y + \boldsymbol{B}_z) && \text{and is perpendicular to } \boldsymbol{T}_{av},\ \boldsymbol{N}_{av} \text{ and } \boldsymbol{D} \\
\circ \quad \boldsymbol{B}_{anti} &= 0.5(\boldsymbol{B}_y - \boldsymbol{B}_z) && \text{used for the local induction estimate in Fig. 4.8}
\end{aligned}
\tag{4.2}
$$

  ○ That is: Subtract the tangent and curvature vectors because they become anti-parallel as $t \nearrow t_r$, and add the bi-normals because they are parallel as $t \nearrow t_r$.
  ○ The average curvature $\boldsymbol{N}_{av}$ is aligned with the separation $\boldsymbol{D}$, while the average tangent $\boldsymbol{T}_{av}$ and average bi-normal $\boldsymbol{B}_{av}$ are orthogonal to $\boldsymbol{D}$.
  ○ The alignments of $\boldsymbol{T}_{av}$, $\boldsymbol{N}_{av}$ and $\boldsymbol{B}_{av}$ with each other and $\boldsymbol{D}$ form in the early stages, long before the reconnection at $t_r = 8.92$.
- Post-reconnection Frenet-Serret flip:
  ○ Figure 4.8 shows that the directions of $\boldsymbol{T}_{av}$ and $\boldsymbol{N}_{av}$ swap and $\boldsymbol{D}$ rotates by 90° so that all three are still in the *reconnection plane* with the same relations to one another.
  ○ $\boldsymbol{B}_{av}$ remains orthogonal to the *reconnection plane*.
  ○ $\boldsymbol{B}_{anti}$ can be used in the local induction approximation (LIA) for the approach of the vortices,

$$
(d\delta_{yz}/dt)_{LIA} = c\Gamma\kappa\boldsymbol{B}_{anti}\,,
\tag{4.3}
$$

and does change its sign from negative (approaching) to positive (separating) at the reconnection time. However, LIA would be a poor approximation for the motion of $\rho \equiv 0$ lines governed by the Gross-Pitaevskii equations. This velocity can be
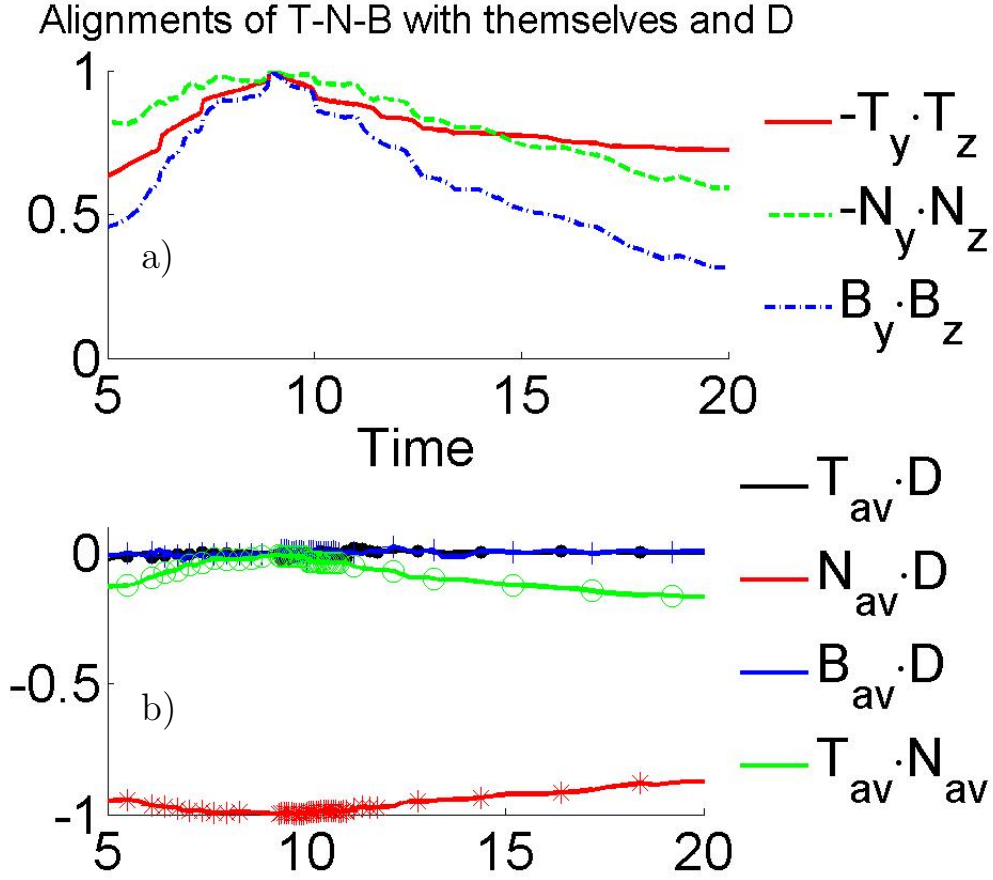
FIGURE 4.7. These two frames show how the basis vectors of the Frenet-Serret frames at $\boldsymbol{x}_{y,z}$ are aligned and help define the *reconnection plane* and the *propagation plane* in Figs. 2.2g,i. a): The alignments between the vortices of their Frenet-Serret components of $\boldsymbol{x}_{y,z}$: Tangents $-\boldsymbol{T}_y \cdot \boldsymbol{T}_z$. Curvature $-\boldsymbol{N}_y \cdot \boldsymbol{N}_z$. And bi-normals $\boldsymbol{B}_y \cdot \boldsymbol{B}_z$. For $t < t_r$ the tangent and curvature vectors become increasingly anti-parallel as the reconnection time is approached while the bi-normal vectors become increasingly aligned. These trends are are reversed for $t > t_r$. b): The alignments between the averages over $\boldsymbol{x}_{y,z}$ of the Frenet-Serret frames defined by (4.2) with the separation vector $\boldsymbol{D}$ between $\boldsymbol{x}_z$ and $\boldsymbol{x}_y$.

expressed explicitly in terms of the $\boldsymbol{\omega}_\psi$, $\nabla\psi$ and $\triangle\psi$ as follows:

$$\frac{d}{dt}\boldsymbol{x}(s,t) = -0.5\frac{\triangle\psi_i(\boldsymbol{\omega}_\psi \times \nabla\psi_i) + \triangle\psi_r(\boldsymbol{\omega}_\psi \times \nabla\psi_i)}{\boldsymbol{\omega}_\psi^2} \ .$$

This formula will be used in a later paper.

The alignments of the components of the Frenet-Serret frames at $\boldsymbol{x}_{y,z}$ and the separation of these points $\boldsymbol{D}$ is significantly different than their alignments for the anti-parallel case in Sec. 5. Comparisons are discussed in the Summary in Sec. 6.

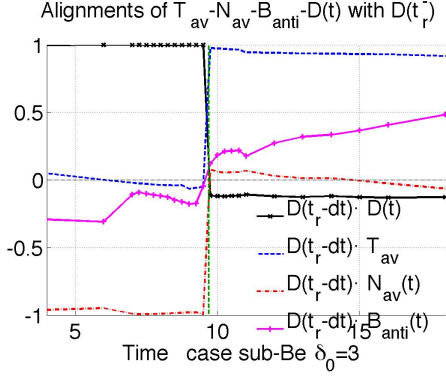FIGURE 4.8. For the $\delta_0 = 3$, 128^3 calculation, the alignments over time of $\boldsymbol{D}(t_r^-)$ with $\boldsymbol{T}_{av}$ and $\boldsymbol{N}_{av}$, the averages (4.2) over the tangent and curvature components of the Frenet-Serret frames at the closest points $\boldsymbol{x}_{y,z}$. $\boldsymbol{B}_{av} \cdot \boldsymbol{D}(t_r^-) \approx 0$ for all times. $\boldsymbol{D}(t_r^-)$ is the separation direction at $t = 9.5$, just before reconnection. Also shown is the alignment of $\boldsymbol{D}(t_r^-)$ with the anti-symmetric part of the bi-normals $\boldsymbol{B}_{anti} = 0.5 * (\boldsymbol{B}_y - \boldsymbol{B}_z)$, which appear in the LIA estimate for how the separation $\delta(t)$ changes in time.
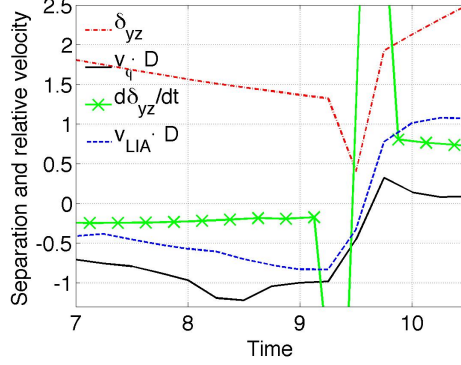
FIGURE 4.9. Alignments between the separation δ_{yz} of y and z vortices and several velocities for the $\delta_0 = 3$, 128^3 test calculation. These include the projected phase velocity $(\boldsymbol{v}_z^\phi - \boldsymbol{v}_y^\phi) \cdot \boldsymbol{D}$, a second-order difference for $d\delta/dt$, and a projected velocity from the local induction approximation: $(\boldsymbol{v}_z^{\text{LIA}} - \boldsymbol{v}_y^{\text{LIA}}) \cdot \boldsymbol{D} = 2\pi\kappa\boldsymbol{B}_{anti} \cdot \boldsymbol{D}$ where $\kappa = \kappa_z = \kappa_y$ at $s = s_0$ is taken from Fig. 4.4, the circulation of the vortex is $\Gamma = 2\pi$ and the anti-symmetric bi-normal $\boldsymbol{B}_{anti}$ (4.2) is used.
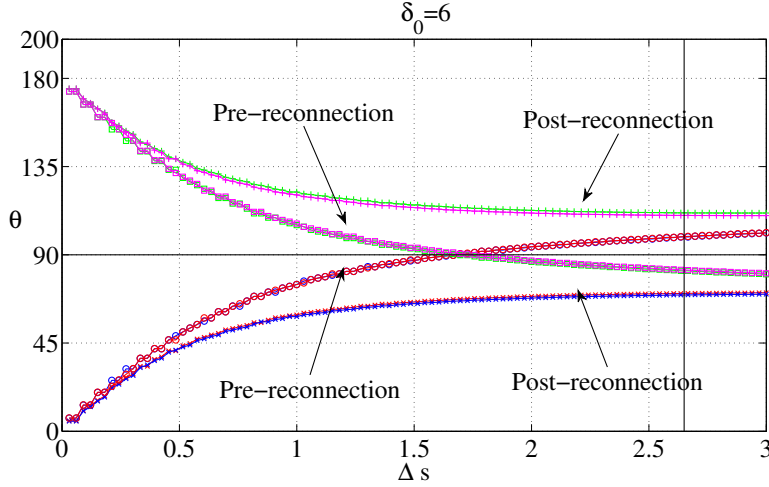

FIGURE 4.10. Angles between the segments in 3D space displayed in Fig. 4.6 as a function of Δs for $\delta_0 = 6$ and $t = 63$ (pre-reconnection) and $t = 65$ (post-reconnection). The angles sum to $360°$ as $\Delta s \to 0$, implying that the segments near the reconnection point $\boldsymbol{x}_r$ lie on a plane, specifically, the reconnection plane in Fig. 4.6 The sum of the angles grows with Δs and is about$\sim 362°$ for $\Delta s \sim 2.6$ (vertical black line), which is consistent with the arms of reconnecting vortices becoming progressively more convex and hyperbolic as they move away from $\boldsymbol{x}_r$, both before and after reconnection. The rapidly changing behavior for small Δs is a kinematic result of how the lines and angles indicated in Fig. 4.6 were chosen and is not significant. What could be more significant are the differences in the angles for intermediate Δs and their influence upon any Biot-Savart contributions to the velocities.

4.5. *Angles at reconnection*

What additional dynamics do we need to identify if we want to explain how the differences in the local Frenet-Serret frames in the orthogonal cases and could lead to the anti-parallel case to the differences in their respective separation scaling laws?

One place to look is larger-scale alignments and long-range interactions. While the underlying Gross-Pitaevskii equations are local, the existence of the vortex structures means that such alignments should exist and should influence the local motion of the $\rho \equiv 0$ lines to the degree that the law of Biot-Savart can be applied. With that goal, this section will determine the evolution of pre- and post-reconnection angles between points on the extended structures.

Angles can be defined between the arms of the reconnecting vortices around the reconnection point as follows.

(*i*) From the points of closest approach $\boldsymbol{x}_{y,z}(t)$, define $\boldsymbol{x}_r(t) = 0.5(\boldsymbol{x}_y(t) + \boldsymbol{x}_z(t))$.

(*ii*) Move $\pm\Delta s$ along the arms of the vortices from $\boldsymbol{x}_{y,z}(t)$ and identify four new points: $\mathbf{x}_{1,y}$, $\mathbf{x}_{2,y}$, $\mathbf{x}_{1,z}$ and $\mathbf{x}_{2,z}$, illustrated in the Nazarenko projection sketch in Fig. 2.2i.

(*iii*) To get a fully three-dimensional perspective, note that these points lie on outstretched arms such as in Fig. 2.2b.

(*iv*) Connect the four points with $\mathbf{x}_r$ to form an extended three-dimensional frame then calculate the angles θ_i between these four vectors.

(*v*) Plots of $\theta_i(\Delta s)$ show qualitatively similar variations independent of δ_0 with these properties:

    ○ The sum of the Δ_i grows as Δs increases, starting from $\sum_i \theta_i(\Delta s = 0) = 360°$.

    ○ This shows that the inner ($\Delta s \approx 0$) structure is a plane.

    ○ $\sum_i \theta_i(\Delta s)$ increases with Δs, implying that the global structure is convex or hyperbolic, the opposite of a structure with an acute angles such as a pyramid.

    ○ The Δs at which the pre-reconnection θ_i cross the $\theta = 90°$ horizontal line increases at δ_0 increases.

    ○ The vertical line in Fig. 4.10 represents the Δs_p for which $\sum_i \theta_i(\Delta s) = 362° > 360°$, indicating that the structure is mildly hyperbolic.

    ○ $\sum_i \theta_i(\Delta s)$ increases as δ_0 decreases. For $\delta_0 = 3$, $\sum_i \theta_i(\Delta s) = 370°$ for large Δs.

    ○ When looking down at the *reconnection plane* in either Fig. 4.6 or Fig. 2.3b, do not forget that the centre of the *reconnection plane* is moving along the $y = z$ direction of the *propagation plane* and simultaneously dragging or pushing the extended arms as it moves, as in Fig. 2.2b.

Understanding these features should provide some hints for the origins of the anomalous scaling laws and be part of the overall explanation. One hint could be the significantly different angles at intermediate scales. That is, pre-reconnection, the $0.5 < \Delta s < 2.5$ span has approximately retained its $\theta \sim 90°$ original orthogonal alignment, which is lost after reconnection for the the post-reconnection angles for this span in Δs. All of the δ_0 cases show similar differences between the pre- and post-reconnection angles over similar Δs spans. From the point of view of non-local Biot-Savart contributions to the velocities, these differences could be significant because the $\theta \approx 90°$ spans might not contribute to the Biot-Savart integrals for the velocities. That is, one could only integrate out to $\Delta s \approx 1$, which would suppress the pre-reconnection velocities.
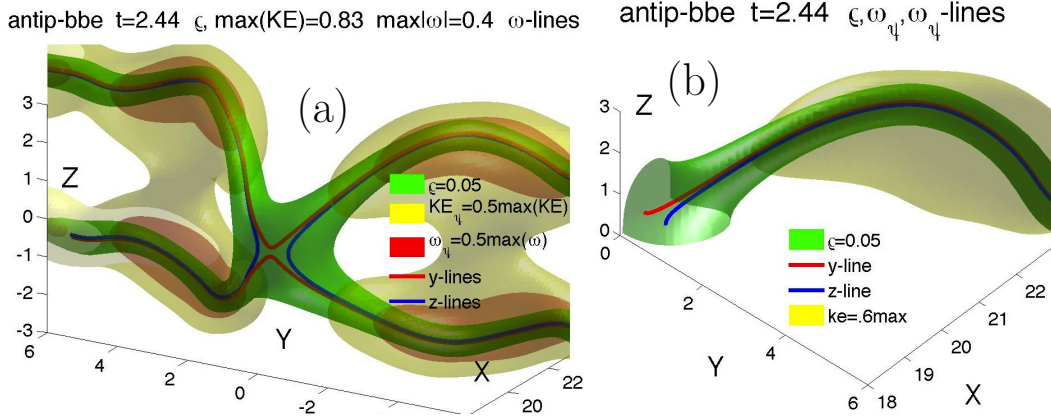
FIGURE 5.1. Density, kinetic energy $K_{\nabla\psi} = 0.5|\nabla\psi|^2$ (2.4) and pseudo-vorticity $|\nabla\psi_r \times \nabla\psi_i|$ isosurfaces plus vortex lines a bit after the time of the first reconnection, $t = 2.4375 \gtrsim t_r = 2.344$ from two perspectives with $\max(K_{\nabla\psi}) = 0.83$. $\max|\omega_\rho| = 0.4$ for all the times. (a) shows four vortex lines, with each pair starting at the points of nearly zero density on the $y = 0$ and $z = 0$ symmetry planes respectively. (b) gives a second perspective that looks into a quadrant through the two symmetry planes and is designed to demonstrate that locally, around $y = z = 0$, the shape of the $\rho = 0.05$ isosurface is symmetric on the two symmetry planes.

5. Anti-parallel results: approach, separation, curvature

In contrast to the orthogonal vortices, whose scaling laws do not obey expectations, it will now be shown that the scaling of initially anti-parallel vortices obeys those expectations almost completely.

Figure 2.1 illustrated the overall structure of our anti-parallel case before reconnection at $t = 0.125$ and after reconnection at $t = 4$, where $t_r \approx 2.44$. The very low density $\rho = 0.05$ isosurface is the primary diagnostic for the vortex lines and as in Kerr (2011), the post-reconnection density isosurfaces are developing a second set of reconnections near $y = \pm 5$ from which the first set of vortex rings will form. Eventually two stacks of vortex rings on either side of $y = 0$ should form from the additional waves along the original vortex lines. Large values of the gradient kinetic energy (2.4) and the magnitude of the pseudovorticity (3.1) are shown using two additional isosurfaces and the trajectories of the $\rho \approx 0$ pseudo-vorticity are traced with thick lines.

Figure 5.1 provides two perspectives of the structure approximately at the reconnection time using the same isosurfaces and vortex lines as in Fig. 2.1, except there are now two sets of vortex lines. Fig. 2.1a shows two red curves seeded using $\rho \approx 0$ points on the $y = 0$, $x - z$ *perturbation plane* and two blue curves seeded using $\rho \approx 0$ points on the $z = 0$, $x - y$ *dividing plane*, representing respectively the pre- and post-reconnection trajectories.

As for the $\delta_0 = 3$ orthogonal case in Fig. 4.3b, the reconnection time isosurfaces have an extended zone of very low density around the reconnection point and a strong isosurface of the gradient kinetic energy outside this zone. Large values of $|\omega_\rho|$ are also outside the reconnection zone.

Figure 5.2 presents several possible fits for the pre- and post-reconnection separation scaling laws, with both the pre-reconnection incoming and post-reconnection outgoing separations following the predicted dimensional scaling of $\delta \sim |t_r - t|^{1/2}$ (1.1), unlike the orthogonal cases just shown. Furthermore, for $\Delta t = |t - t_r| < 0.5$, the $\delta_{\text{in}}(t_r - t)$ and

$\delta_{\text{out}}(t_r - t)$ are almost mirror images of each other. Although that is not the case for larger Δt.

This suggests that unlike the orthogonal case, where we have attempted to relate the asymmetric scaling laws to asymmetries in the underlying structure, for the anti-parallel case we want to identify physical symmetries that would predispose the scaling laws to be temporally symmetric and follow the dimensional prediction.

The purpose of giving two perspectives near the reconnection time in Fig. 5.1 is to clarify the physical symmetries at this time. The overall structure in Fig. 5.1a shows how all four legs of vorticity converge on the $y = z = 0$ line where the $x - z$ or $x - y$ symmetry planes cross. Then Fig. 5.1b looks at the structure from the inside, from the perspective of the line where the symmetry planes meet. This shows how the zone of nearly zero density crosses both symmetry planes and provides the seeds for generating the butterfly trajectories around the $y = z = 0$ line in Fig. 5.1a.

A useful, but not perfect, way to characterise the resulting structure is to use the proposal by de Waele & Aarts (1994), based on their Biot-Savart calculation of anti-parallel quantum vortices, that near reconnection the vortices form an equilateral pyramid. The pyramid for Fig. 5.1a can be formed by straightening the 2 red and 2 blue curved legs of vorticity surrounding the $y = z = 0$ line in x to $(x, y, z) \approx (18, 0, 0)$, slightly to the left of the $\rho = 0.05$ isosurface. These extensions would start from tangents to the red and blue lines. The angles θ_{yz} of these tangents with respect to the symmetry planes would define the sharpness of the tip of pyramid and depend where the tangents are taken from. $\theta_{y,z} = 45°$ is obtained for $|y| = |z| \leq 2$, which is where the vortices begin to bend back upon themselves.

Why don't the pseudo-vortex lines continue to bend, or kink, until a sharp tip with $\theta_{y,z} = 45°$ is obtained? Figure 5.3 provides the clues by directly plotting the curvatures and the inclinations of the tips of the y and z pseudo-vortex lines, which are the points of closest approach in Fig. 5.3a. The curvatures are determined by (3.4) and the inclinations come from $\boldsymbol{N} = (n_x, n_y, n_z)$, the direction of the curvature from (3.3b). Independent of whether one considers the red y-vortices or blue z-vortices, their maximum curvatures have nearly the same upper bounds and the same maxima as $n_{y,z}/n_x$, with $n_z/n_x \nearrow 6$ as $t \nearrow t_r$ for $t > t_r$ and $n_y/n_x \searrow 6$ as $t \searrow t_r$. $\tan\theta_{\pm} = 6$ corresponds to $80°$, not the $45°$ angles of a pyramid.

This means that as reconnection is approached, the direction of the curvature $\boldsymbol{N}$ begins to be parallel to their separation $\boldsymbol{D}$, very reminiscent of what has been found for the orthogonal vortices as $t \to t_r$ in Figs. 4.7 and 4.8. Which also means that the directions of the curvature and tangents nearly swap during reconnection, which is also similar to, but not exactly the same as, the orthogonal cases. And not what a true pyramid with a sharp tip would do.

What is probably more important for getting the dimensional scaling for $\delta(t)$ is that both sets of curves are temporally symmetric. That is, $\kappa(t_r - t) \approx \kappa(t - t_r)$ and $n_z(t_r - t)/n_x(t_r - t) \approx n_y(t - t_r)/n_x(t - t_r)$. Fig. 5.3b emphasises this further by showing the dependence of κ_y and κ_z on their arclengths s at times just before and after the estimated reconnection time of $t_r = 2.34$.

Finally, let us go back to the three-dimensional structures. First, consider how the $t < t_r$ vortex lines in Fig. 2.1a evolve into the pinched red y-vortex lines in Fig. 5.1a along a path in the $x - z$ symmetry plane with $(n_x, 0, n_z)(t) = (\cos\theta_-, 0, \sin\theta_-) \nearrow (\cos 80°, 0, \sin 80°)$. Then note that the process is reversed for $t > t_r$ as the pinch in the blue z-vortex lines relaxes in z as $\delta_+ \searrow 0$ along a path in the $x - z$ symmetry plane from its most extreme orientation: $(n_x, n_y, 0)(t) = (\cos\theta_+, \sin\theta_+, 0) \searrow (\cos 80°, \sin 80°, 0)$.
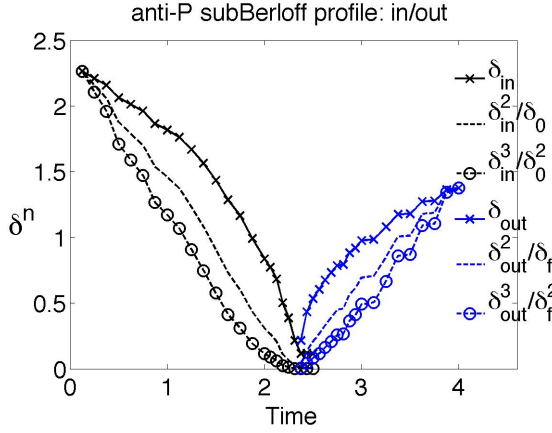
FIGURE 5.2. Separations near the time of the first reconnection of the anti-parallel vortices. The positions are found using the isosurface method on the symmetry planes. Both pre- and post-reconnection curves (*in* and *out*) follow $\delta_0 \sim (t_r - t)^{1/2}$ most closely.
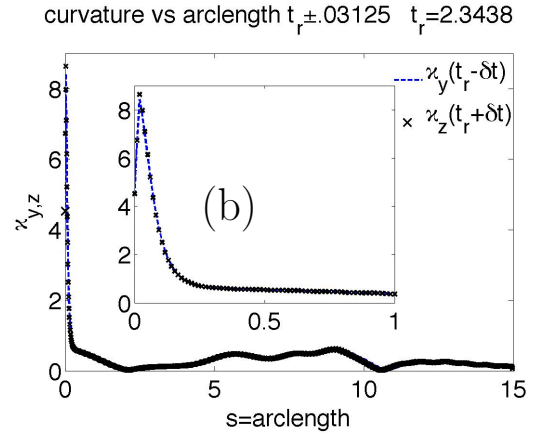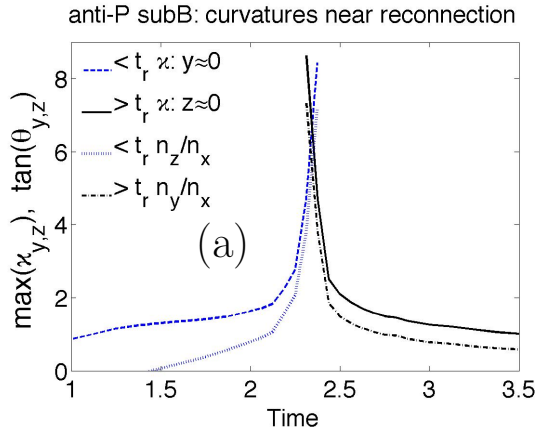

FIGURE 5.3. a: Maximum curvatures, κ_{y0}, κ_{z0}, versus time. κ_{y0} and κ_{z0} are always on symmetry planes. The approach before reconnection and separation after reconnection are similar. Reconnection time is where the curves cross, $t_r \approx 2.344$. b: Curvatures as a function of arclength along the vortices near the reconnection time, with the profile from the new z vortex taken a bit before t_r and the profile of the old y vortex a bit after t_r. The curavatures near $y = z = 0$ are similar, which drives similar approach and separation velocities.

Therefore the evolution of the in and out angles is temporally symmetric, as hoped for, even though the tip is smooth, unlike a true pyramid.

These results differ from the anti-parallel case in Zuccher *et al.* (2012), which shows a slower approach and faster separation, similar to the scaling observed for a recent anti-parallel Navier-Stokes calculation (Hussain & Duraisamy 2011). There could be several reasons for the differences. First, the initial perturbations to the anti-parallel trajectories in Zuccher *et al.* (2012) are pointed towards one another, and not in the direction of propagation as here. Another difference is that their periodic boundaries in y (the vortical direction) are relatively close, unlike that direction here. In Kerr (2011) and in a recent set of Navier-Stokes reconnection calculations Kerr (2013c), the advantages of making that direction very long are discussed.

6. Summary

The reconnection scalings of two configurations of paired vortices, orthogonal and anti-parallel, have been found to have different scaling exponents.

For the anti-parallel case, the temporal scaling of both the pre- and post-reconnection separations obey the dimensional prediction, $\delta_\pm(t) \sim A\sqrt{\Gamma|t_r - t|}$ and the arms of the vortex pairs as the reconnection time is approached form an equilateral pyramid with a smooth tip, which is in most respects qualitatively similar to the prediction of a Biot-Savart model (de Waele & Aarts 1994). Except that around the smooth tip the curvatures $\boldsymbol{N}$ and separation $\boldsymbol{D}$ are nearly parallel and as a result the directions of curvature $\boldsymbol{N}$ and the tangents $\boldsymbol{T}$ almost swap during reconnection.

The orthogonal cases, in contrast, all cases show an asymmetric temporal scaling with respect to the reconnection time t_r cases , For $t < t_r$, $\delta_-(t) \sim A_-(\Gamma|t_r - t|)^{1/3}$ and for $t > t_r$, $\delta_+(t) \sim A_+(\Gamma|t_r - t|)^{2/3}$, where the coefficients $A_\pm$ are independent of the initial separation δ_0. At $t \approx t_r$, the reconnecting vortices are anti-parallel, with the vortices interacting in a *reconnection plane* that contains the tangent and curvature vectors of both vortices as well as their separation vector, which results in the directions of curvature and vorticity swapping during reconnection.

Two innovations What made these calculations and their clean analysis possible were two innovations. One an initial core profile that seems to absorb the unphysical waves that the interacting vortices generate. Second a way to trace the vortex lines that does not require identifying computational cells with small values of the density.

6.1. *Contrasting geometries*

Based on the results presented, for $t \approx t_r$ near the reconnection in the $\boldsymbol{x}_r$ zone immediately around the reconnection point, there are more similarities than originally thought. The curvature vectors align with the separation between the vortices, exactly in the orthogonal cases, and the the opposite vortices are anti-parallel, even for the orthogonal cases where there are no symmetries to impose this property. Post-reconnection, in both cases the curvature and tangent directions swap, or nearly so in the anti-parallel case.

This also means that in neither case does a pyramid form in the zone immediately around $\boldsymbol{x}_r$. Nor do any of the fixed point solutions identified in Meichle *et al.* (2012) form, although there are some similarities between the motion post-reconnection orthogonal vortices and the motion coming out their four half-infinite vortex case.

However, further from $\boldsymbol{x}_r$, the situation is different. For the orthogonal cases, angles between the vortices imply a convex or hyperbolic structure, which in the anti-parallel case a pyramid forms with acute angles.

Let us summarise the additional key features of the orthogonal cases.

Orthogonal For the initially orthogonal vortices, from an early time the directions of vorticity at their points of closest approach gradually become anti-parallel and their respective curvature vectors gradually become anti-aligned with the line of separation. Combined, this implies that the local bi-normals for each line are nearly parallel and do not point in the direction of separation. At reconnection, the directions of the vorticity and curvature swap, and the sign of the bi-normal reverses. All of this is in a *reconnection plane* defined by the averages of the curvature and vorticity directions at the points of closest approach.

Despite the bi-normal being nearly perpendicular to the separation direction, until the time of reconnection, the components of both the phase velocity and a local induction velocity along their separation are consistent with how the separation decreases. A new algorithm for the velocities of the $\rho \equiv 0$ lines (3.2) is introduced, but not used here, and could in ongoing analysis clarify this.

Another useful perspective is the Nazarenko projection in Fig. 2.3, which is along a 45° angle in the $y - z$ plane. From this perspective, the vortices are always distinct, without any loops, and one can see that the pre-reconnection vortices approach the reconnection from one direction, and post-reconnection vortices separate in another. This projection is used for finding non-local alignments and angles as in Fig. 4.10, which show that the global alignment of the initial orthogonal vortices is hyperbolic.

While the three-dimensional graphics for our orthogonal cases are qualitatively similar to the equivalent Gross-Pitaevskii density isosurfaces in Zuccher *et al.* (2012), our interpretation of the underlying geometry is different. Zuccher *et al.* (2012) conclude that the deviations of Gross-Pitaevskii separations from the dimensional prediction is only near the reconnection and probably due to the rarefaction waves they report.

Our conclusion is that the new scaling laws appear at all times for initially orthogonal vortices and these scaling laws are probably tied to the unique alignment of the Frenet-Serret frames that form early and continue through the reconnection period until to the end of each calculation. These conclusions are only possible because of the two innovations that gave us smooth separation curves and allowed us to calculate the properties of the Frenet-Serret frames. That these anomalous scaling laws are identical, about their respective reconnection times, for all initial separations, implies that the anomalous scaling laws could exist for initial vortices with macroscopic initial separations extending to observable scales.

7. Discussion

These results leave two major questions. First, could one use the new orthogonal Frenet-Serret alignments to explain their scaling laws? An explanation that should include why the anti-parallel case qualitatively does what the Biot-Savart calculation of de Waele & Aarts (1994) and dimensional analysis suggested.

Second, are these two cases sufficient for characterising all quantum reconnections events in quantum fluids? Several additional curved configurations were considered in Rorai (2012) that were between the orthogonal and anti-parallel cases discussed here. Depending on the relative initial angles and initial separations of the curved vortices, each case showed temporal scaling that was a mix of distinct scalings described for the orthogonal and anti-parallel cases. These results, plus the cases of Zuccher *et al.* (2012), suggest that the scaling of all quantum reconnection events should lie between the two extremes presented here.

This paper has considered only the scaling of single reconnection events and does not consider what the distribution of reconnection scaling would be in quantum turbulence or the larger role of reconnection in forming a quantum vortex tangle. The next step, after considering more individual cases, should be to determine the distribution of the scaling around reconnection events in a vortex tangle. Several approaches have been used for generating tangles in Gross-Pitaevskii calculations. One is to start with symmetric initial conditions similar to the classical Taylor-Green vortex (Nore *et al.* 1997; Yepez *et al.* 2009). Another is to shoot vortex rings together (Leadbeater *et al.* 2003; Kerr 2011). What would be expected if the new vortex line analysis introduced here were applied?

Based on the cases presented here, there could be three possibilities. First, distributions that are spread over the whole range between the two extremes, anti-parallel and orthogonal. Second, the statistics could be dominated by the anti-parallel, *dimensional scaling*. There is at least one Biot-Savart calculation that shows that from a variety of initial alignments (except nearly parallel), the vortices will be drawn out to be anti-parallel, from which scaling consistent with the dimensional prediction appears (Siggia

1985). Third, it is also possible that the orthogonal scaling could dominate if non-local effects from asymmetries in the geometry tend to dominate their motion.

What do the experiments using solid hydrogen as markers tell us? Associated movies clearly show that post-reconnection separation is faster than the approaches. However, neither of the papers with analysis of the separation statistics sees this effect. For the first report (Bewley *et al.* 2008), this is simply because they did not show post-reconnection scaling, while the more recent work Paoletti *et al.* (2008) shows both pre- and post-reconnection scaling, but these are both clustered about the dimensional prediction. So until there are more experiments, the question of which statistics dominates will remain open.

Acknowledgements

REFERENCES

ALAMRI, S.Z., YOUD, A.J., & BARENGHI, C.F. 2008 Reconnection of superfluid vortex bundles *Phys. Rev. Lett.* **101**, 215302.

BARENGHI, CF 2008 Is the Reynolds number infinite in superfluid turbulence? *Physica D* **237**, 2195-2202.

BERLOFF, N.G. 2004 Interactions of vortices with rarefaction solitary waves in a Bose-Einstein condensate and their role in the decay of superfluid turbulence *Phys. Rev. A* **69**, 053601.

BERLOFF, N.G. 2004 Padé approximations of solitary wave solutions of the GrossPitaevskii equation *J. Phys. A* **37**, 16171632.

BEWLEY, G.P., PAOLETTI, M. S., SREENIVASAN, K. R., & LATHROP, D. P. 2008 Characterization of reconnecting vortices in superfluid helium *Proc. Nat. Aca. Sci.* **105**, 1370713710.

BORATAV, O.N., PELZ, R.B., & ZABUSKY, N.J. 92 Reconnection in orthogonally interacting vortex tubes: Direct numerical simulations and quantification in orthogonally interacting vortices *Phys. Fluids A* **4**, 581605.

DE WAELE, A.T.A.M, & AARTS, R.G.K.M. 1994 Route to vortex reconnection *Phys. Rev. Lett.* **72**, 482485.

FETTER, A. L. 1969 . In *Lectures in Theoretical Physics: Quantum Fluids and Nuclear Matter, volume XIB* (ed. K. T. Mahanthappa and W. E. Brittin), pp. 351-. Gordon & Breach Science Pub, New York.

KERR, R.M. 1985 Higher order derivative correlations and the alignment of small–scale structures in isotropic numerical turbulence. *J. Fluid Mech.* **153**, 31.

KERR, R.M. 2011 Vortex stretching as a mechanism for quantum kinetic energy decay *Phys. Rev. Lett.* **106**, 224501.

KERR, R.M. 2013a Swirling, turbulent vortex rings formed from a chain reaction of reconnection events *Phys. Fluids* **25**, 065101.

KERR, R.M. 2013b Bounds for Euler from vorticity moments and line divergence *J. Fluid Mech* **729**, R2.

KERR, R.M. 2013c Fully developed hydrodynamic turbulence from a chain reaction of reconnection events. In *Procedia IUTAM Understanding Common Aspects of Extreme Events in Fluids, University College Dublin, Dublin, Ireland, 2-6 July 2012.* (ed. M.D. Bustamante, A.C. Newell, R.M. Kerr, M. Tsubota), pp. 57—68. Elsevier, *Procedia IUTAM*, **9**. http://www.sciencedirect.com/science/journal/22109838/9

KOPLIK, J., & LEVINE, H. 1993 Vortex reconnection in superfluid helium *Phys. Rev. Lett.* **71**, 13751378.

Kozik, B., & Svistunov, B. 2004 Kelvin-wave cascade and decay of superfluid turbulence *Phys. Rev. Lett.* **92**, 035301.

Hussain, F., & Duraisamy, K. 2011 Mechanics of viscous vortex reconnection *Phys. Fluids* **23**, 021701.

Kursa, M., Bajer, K., & Lipniacki, T. 2011 Cascade of vortex loops initiated by a single reconnection of quantum vortices *Phys. Rev. B* **83**, 014505.

Leadbeater, M., Winiecki, T., Samuels, D. C., Barenghi, C. F., & Adams, C. S. 2001 Sound Emission due to Superfluid Vortex Reconnections *Phys. Rev. Lett.* **86**, 14101413.

Leadbeater, M., Samuels, D. C., Barenghi, C. F., & Adams, C. S. 2003 Decay of superfluid turbulence via Kelvin-wave radiation *Phys. Rev. A* **67**, 015601.

Meichle, D.P., Rorai, C., Fisher, M.E., & Lathrop, D.P. 2012 Quantized vortex reconnection: Fixed points and initial conditions *Phys. Rev. B* **86**, 014509.

Nazarenko, S., & West, R. 2003 Analytical solution for nonlinear Schrödinger vortex reconnection *J. Low Temp. Phys.* **132**, 1–10.

Nore, C., Abid, M., & Brachet, M.E. 1997 Kolmogorov Turbulence in Low-Temperature Superflows *Phys. Rev. Lett.* **78**, 3896.; 1997 Decaying Kolmogorov turbulence in a model of superflow *Phys. Fluids* **9**, 26442669.

Paoletti, M. S., Fisher, M. E., Sreenivasan, K. R., & Lathrop, D. P. 2008 Velocity statistics distinguish quantum from classical turbulence *Phys. Rev. Lett.* **101**, 154501.

Rorai, C. 2012 *Vortex reconnection in superfluid helium*. University of Trieste.

Rorai, C., Sreenivasan, K. R., & Fisher, M. E. 2013 Propagating and annihilating vortex dipoles in the Gross-Pitaevskii equation *Phys. Rev. B* **88**, 134522.

Sasa, N., Kano, T., Machida, M., L'vov, V.S., Rudenko, O., & Tsubota, M. 2011 Energy spectra of quantum turbulence: Large-scale simulation and modeling *Phys. Rev. B* **84**, 054525.

Schwarzschild, B. 2010 Three-dimensional vortex dynamics in superfluid ^{4}He: Homogeneous superfluid turbulence *Phys. Today* **July 2010**, 1214.

Siggia, E. 1985 Collapse and amplification of a vortex filament *Phys. Fluids* **28**, 794–805.

Skrbek, L., & Sreenivasan, K. Phys. Fluids *24* **011301**, Developed quantum turbulence and its decay.

Svistunov, B.V. 1995 Superfluid turbulence in the low-temperature limit *PRB* **52**, 3647.

Walmsley, P.M, & Golov, A.I. 2008 Quantum and Quasiclassical Types of Superfluid Turbulence *Phys. Rev. Lett.* **100**, 245301.

Yepez, J., Vahala, G., Vahala, L., & Soe, M. 2009 Superfluid Turbulence from Quantum Kelvin Wave to Classical Kolmogorov Cascades *Phys. Rev. Lett.* **103**, 084501.

Zuccher, S., Caliari, M., & Baggaley, A.W.C.F.Barenghi 2012 arXiv:0911.1733v2 Quantum vortex reconnections.